PROCEEDINGS, 48th Workshop on Geothermal Reservoir Engineering
Stanford University, Stanford, California, February 6-8, 2023
SGP-TR-224

Towards subsurface stress and strain monitoring at the Patua geothermal field

Nori Nakata[1], Don W. Vasco[1], Michelle Robertson[1], Chet Hopp[1], Hongrui Qiu[1], Torquil Smith[1], Eric Sonnenthal[1], Trenton Cladouhos[2], Michael Swyer[3]

[1]Earth and Environmental Sciences Area, Lawrence Berkeley National Laboratory, 1 Cyclotron Rd., Berkeley, CA 94720

[2]Formaly; Cyrq Energy, Salt Lake City, Utah

[3]Cyrq Energy, Salt Lake City, Utah

nnakata@lbl.gov

Keywords: structural monitoring, stress and strain, seismic, geodesy, Patua geothermal field

ABSTRACT

Geothermal resources have the potential to provide clean energy, and the understanding of subsurface stress and strain changes becomes crucial for geothermal operations. We demonstrate the effort to combine seismic (earthquakes and ambient noise), surface deformation (InSAR and GPS) and numerical modeling for characterizing subsurface stress and strain. We have deployed five shallow-borehole seismometers for monitoring the microearthquake activities at the Patua Geothermal Field since June 2021. Patua is a conventional (non EGS) geothermal field; however, the field has a potential to apply a near-field EGS well stimulation to stimulate the reservoir. This local array lowers the magnitude completeness of earthquake detection, which can characterize fault distribution and their criticalness, as well as records ambient-noise data to detect time-lapse changes of subsurface velocities using coda-wave interferometry. Time-lapse changes in velocities provide a unique view of subsurface elastic changes between each receiver pair. Surface deformation estimated from InSAR shows a clear trend of subsidence in addition to the annual cycle. The cumulative deformation from 2018 to 2022 correlates with mapped faults, which suggests that the north-northeast trending faults may be permeable pathways. We will jointly interpret the results of seismic and surface deformation for subsurface stress changes, which could be used for the numerical modeling of future well stimulation activities and evaluating fluid migration within the existing geothermal field.

1. INTRODUCTION

Understanding the detailed stress and strain states in the reservoir and surrounding structure is crucial for mitigating large induced seismicity and reservoir management in geothermal fields. This is especially important when we increase the usage of geothermal resources. In this study, we demonstrate the characterization of stress states at the Patua geothermal field in Nevada (Combs et al., 2012; Garg et al., 2015; Murphy et al., 2017; Cladouhos et al., 2017; Pollack et al., 2021) by combining seismic observations, structural monitoring with seismic and geodesy data, and Thermal-Hydrological-Mechanical-Chemical (THMC) modeling. We combine data-driven and physics-based approaches for understanding the subsurface stress. The seismic observation and ambient noise analysis provide subsurface S-wave velocities at each depth and their time-lapse changes. The low-wavenumber surface deformation obtained by InSAR is related to physical changes in the reservoir, and we estimate volume changes by inverting the deformation. The THMC modeling can numerically model the subsurface fluid flow and stress changes (Smith et al., 2023). In this study, we present results from each analysis and discuss how we can combine them for more comprehensive monitoring of subsurface stress and strain states.

2. SEISMIC OBSERVATIONS

From July 2012 until the end of 2013, a seismic network of 18 borehole-installed 15-Hz geophones was operated at Patua. Most of the equipment was removed after 2013, but many of the geophones were either permanently grouted in place, or were left locked in the boreholes. In June of 2021, in preparation for new DOE-funded projects set to begin at Patua, a team from LBNL began reinstalling recording equipment at many of these sites and testing the functionality of the preexisting downhole geophones. At each site, we also installed a 2-Hz geophone near the wellhead to help characterize the attenuation properties of the surface sediments covering the reservoir. From June 16, 2021 until present, we have recorded data from six of the original 18 sensors and found five to still be functioning (Figure 1). Data were recorded continuously at 500 Hz for both the surface and downhole geophones at each site. Due to issues with snow-covered solar panels and faulty recorders, a minimum of four and maximum of five sites were operational at any one time throughout the dataset. The downhole sensor at site 4509, while functioning, is suspected to be poorly coupled and have multiple bad components, so the recording equipment was relocated to site 23A-17 on January 17, 2022. All other borehole sensors appear to be functioning normally.

The first priority of the seismic network at Patua is to detect and precisely locate as many earthquakes as possible. The more seismicity the network can detect, the better it is able to help mitigate the risk of larger-magnitude events and the more completely it can illuminate seismically active structures in the reservoir. These structures are often key features of the reservoir model as they often serve as either flow pathways or flow baffles and are therefore critical to identify. The Patua network, when using up to 18 borehole sensors, had a magnitude of completeness of roughly 0.0, meaning that it was able to detect all seismicity with a magnitude of >0.0 (or slip on a fracture with a radius of ~5-10 m).

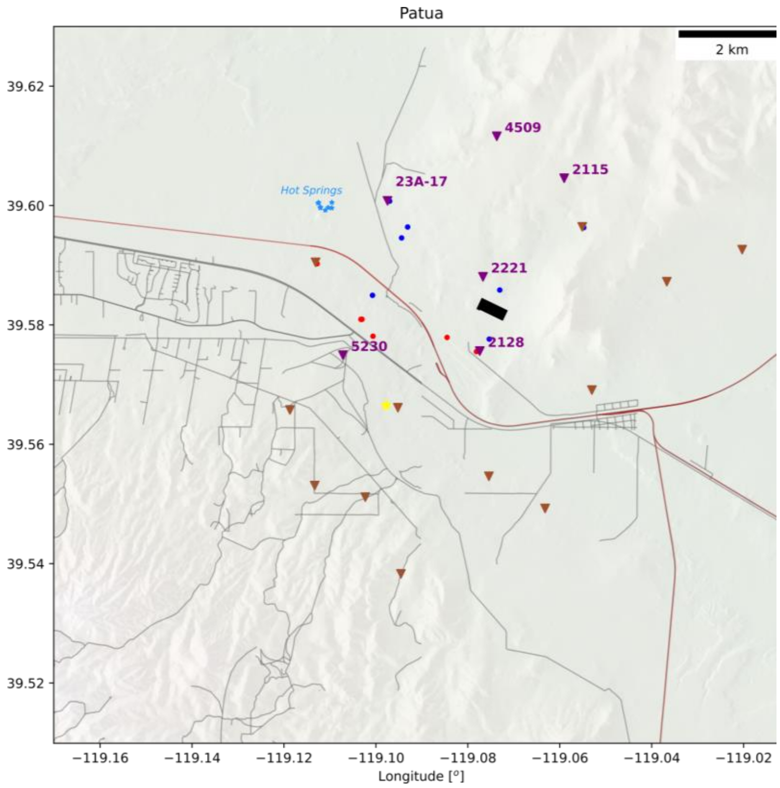

Figure 1: Overview of the Patua geothermal field indicating the locations of previous seismic network sites (brown triangles) and sites that have been reoccupied at some point in the last two years (purple triangles). The location of the proposed stimulation well is shown as a yellow star and the power plant is shown at a black rectangle. Red and blue dots signify production and injection boreholes respectively.

3. SEISMIC AMBIENT NOISE ANALYSIS

We analyze continuous recordings from five pairs of co-located surface and shallow-borehole seismometers deployed at the Patua geothermal field between June 2021 and May 2022. The ambient-noise data recorded by this local array is used to detect time-lapse changes of subsurface velocities using coda-wave interferometry. To do so, we first preprocess the daily recording following the procedure of Bensen et al. (2007). Figure 2 shows the preprocessing procedure for a vertical recording at a specific day from an example station 2221. It is interesting to note that the amplitudes for waves recorded at the low frequency band (0.1-1 Hz) are much (~3 order of magnitude) smaller than those at the high frequency band (1-10 Hz). Thus, we preprocess the data for the low (0.1-1 Hz) and the high (1-10 Hz) frequency bands, separately.

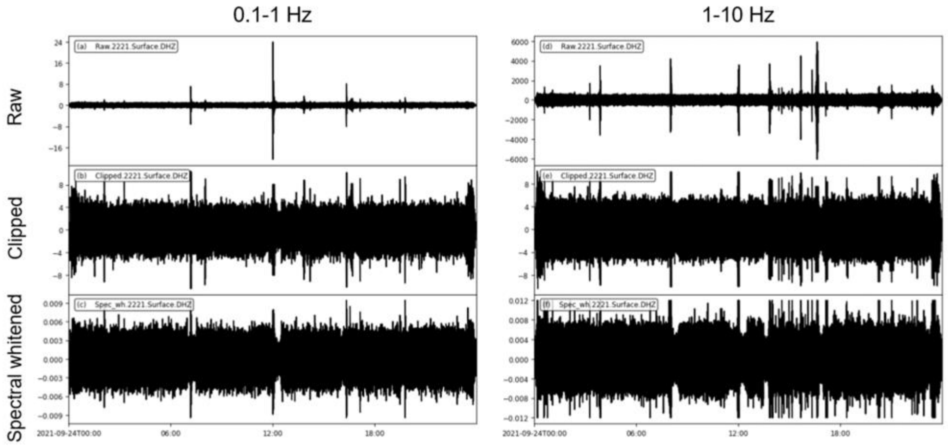

Figure 2: The vertical component daily recording at 2021-09-24 for station 2221 filtered at (a) 0.1-1 Hz and (d) 1-10 Hz. Following the procedure of Bensen et al. (2007), clipping (b, e) and spectral whitening (c, f) are applied to the filtered continuous recording before coda wave interferometry. A 30-min-long moving window is used in the preprocessing.

Figure 3 demonstrates the amplitude spectra of every 5-min-long window of the data before (top) and after (bottom) the spectral whitening. The amplitude spectra show certain shapes in both the low and high frequency bands. This is particularly clear for the high frequency band, where several strong peaks are observed between 4-6 Hz. The observed pattern may relate to either the excitation mechanism of the noise sources or the local structure beneath the station (e.g., reflections from horizontal interfaces) or both. Such pattern can potentially be used to constrain structures of the shallow materials or properties of ambient noise sources at Patua. Since the focus of this study is to monitor changes in subsurface velocities, we suppress such patterns via spectral whitening.

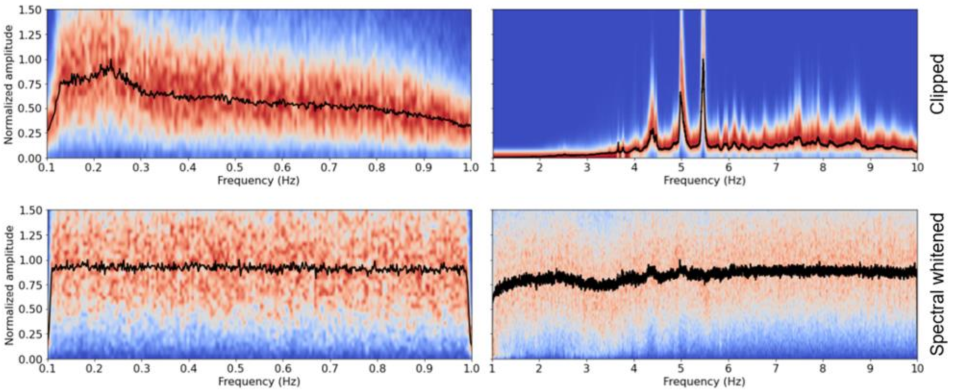

Figure 3: Amplitude-frequency probability density maps of data shown in Figure 2 at low (left) and high (right) frequency bands. Results computed for data before and after the spectral whitening are shown in the top and bottom panels, respectively. Warmer colors indicate larger amplitudes. The black curve illustrates the mean of all the amplitude spectra.

We then cross correlate the preprocessed daily recordings for each station pair and component combinations. Since there are also borehole stations, we also compute daily ambient noise cross correlations (ANCs) for pairs of borehole stations, but only in the high frequency band (1-10 Hz), as these are 15-Hz sensors. Figure 4 illustrates the daily ANCs computed for an example station pair 2128-2221 at vertical-vertical (ZZ) component. Clear and coherent coda waves are observed in daily ANCs at the high frequency band, whereas the coda waves at the low frequency band are much noisier. Thus, we further improve the quality of coda waves in daily ANCs at the low frequency band using moving average. A stacking size of 21 days (i.e., 10 days before and after) is used through trial-and-error analysis.

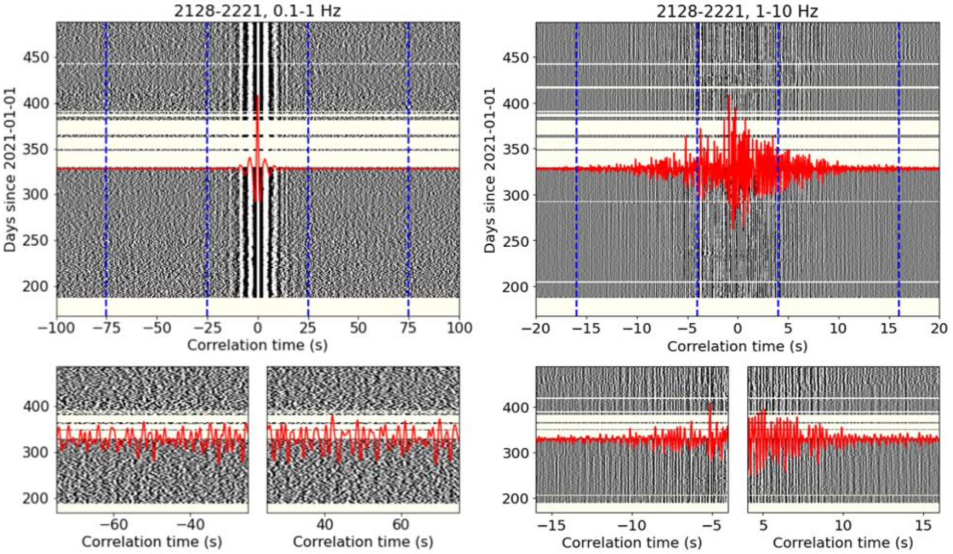

Figure 4: Daily ambient noise cross correlations (ANCs) for station pair 2128-2221 over the entire recording period computed for the low (left) and high (right) frequency bands. The coda waves used to detect subsurface velocity changes are outlined by the blue dashed lines and zoomed in at the bottom panels.

In the next step, we estimate relative travel time changes (*dt/t*) using the time-domain stretching method (Lobkis and Weaver 2003). The stretching method dilates or compress a test trace to fit with a reference trace in time domain and assume that temporal perturbations in coda wave traveltimes are small. Figure 5 demonstrates the calculation of *dt/t* for coda waves narrow bandpass filtered between 1-2 Hz using the example station pair (2128-2221) at ZZ component. Although the coda waves filtered between 1-2 Hz are visually coherent, we still observe clear incoherence noise (Figs. 5c-d) that increase the uncertainty of *dt/t* measurements (Fig. 5b). Here, we denoise the coda waves using a well-developed SVD-based Wiener filter (Moreau et al. 2017). After denoising, the signal to noise ratio of coda waves is much higher (Figs. 5g-h), resulting in higher coherence values (Fig. 5e) and smaller uncertainty values (Fig. 5f).

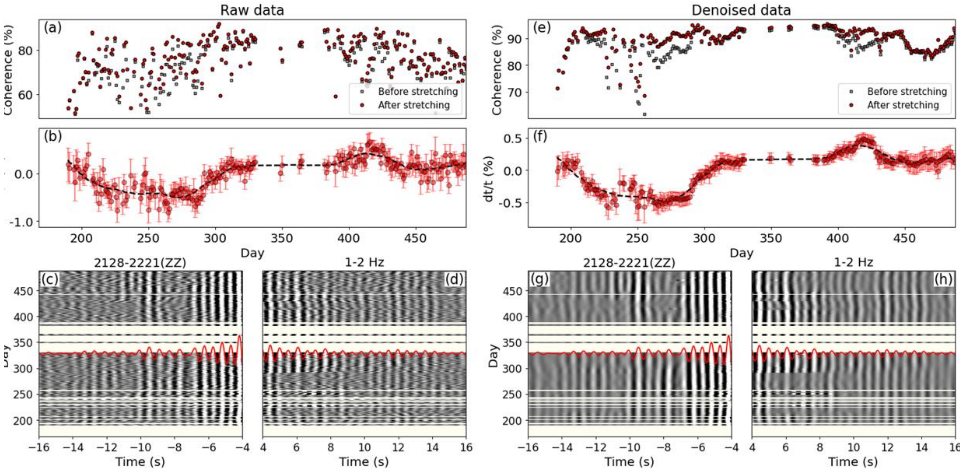

Figure 5: Relative travel time changes (*dt/t*) measured using coda waves before (left) and after (right) denoising. The bottom panels display the coda waves at both positive and negative time lags, whereas the top panels illustrate the coherence and *dt/t* measured by comparing each daily ANC with the mean.

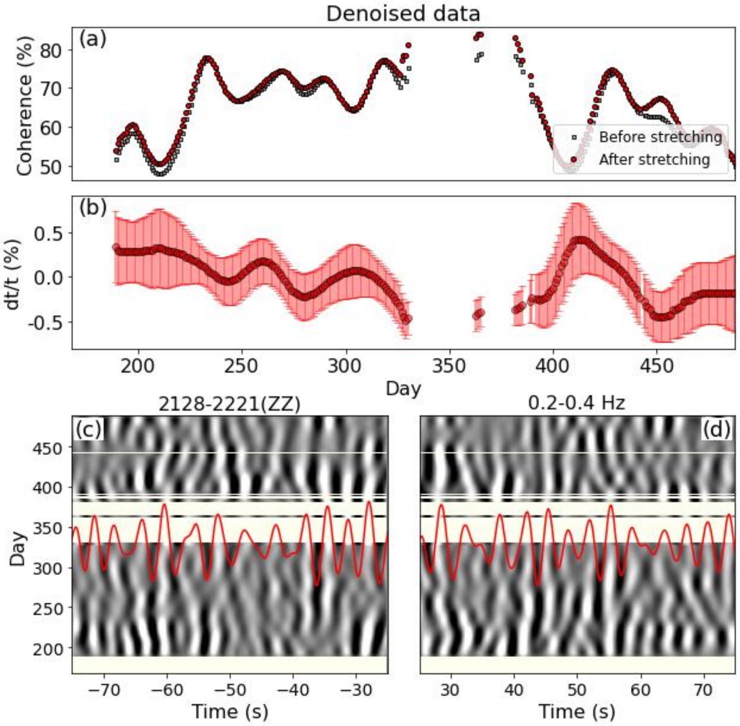

Figure 6: *dt/t* measured using coda waves filtered at a low frequency band (0.2-0.4 Hz). Same as Figs. 5e-h for a lower frequency band.

Figure 6 shows the dt/t measured at a low frequency band (0.2-0.4 Hz). Although the running average and denoising process greatly improve the quality of the coda waves (Figs. 6c-d), the coherence values (Fig. 6a) are still generally lower than those at frequencies higher than 1 Hz (e.g., Fig. 5e) and thus larger uncertainties are observed for the resulting *dt/t* values (Fig. 6b). Therefore, we first discuss the *dt/t* measurements at frequencies higher than 1 Hz (Fig. 7), as these results are derived from data with higher quality and thus more reliable, and then briefly go through the results at frequencies lower than 1 Hz (Fig. 8).

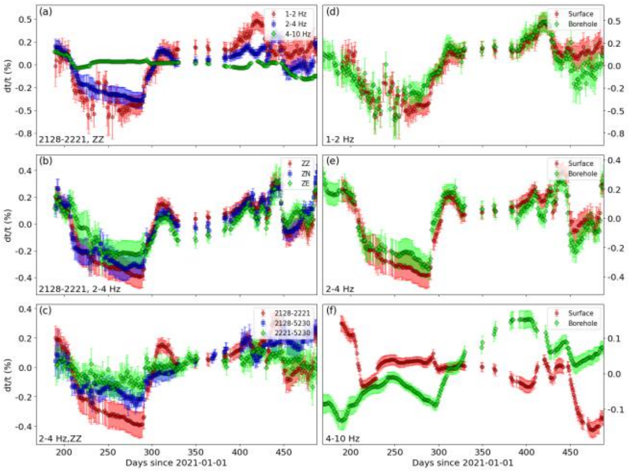

Figure 7: Comparative analysis of *dt/t* curves measured using coda waves at the high frequency band (1-10 Hz) for (a) different frequency bands, (b) components, and (c) station pairs. (d)-(f) show the comparison between *dt/t* obtained from surface (red) and borehole (green) stations.

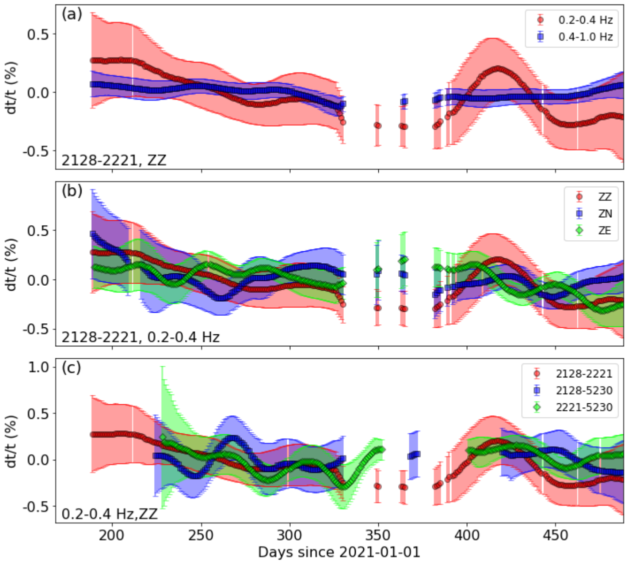

Figure 8: Comparative analysis of *dt/t* curves measured using coda waves at the low frequency band (0.1-1 Hz) for (a) different frequency bands, (b) components, and (c) station pairs. Same as Figs. 7a-c for the low frequency band.

We note that *dt/t* can be measured using coda waves computed for different combinations of station pairs, components, and frequency bands. Since there are more than 100 *dt/t* curves, we first compare the results computed for different frequency bands using the example surface station pair 2128-2221 at ZZ component. As shown in Fig. 7a, the *dt/t* vary within a ~1-2% range and larger peak to peak amplitudes are observed in *dt/t* measured at lower frequency bands (1-2 Hz and 2-4 Hz). This likely indicates that the observed velocity changes occurred at a depth range below the sensitivity of the coda waves at 4-10 Hz recorded by surface stations. Moreover, we also see a change in the long-term trend of *dt/t* between frequency bands. In general, the long-term trend decreases with increasing frequency, suggesting the subsurface velocities are likely decreasing slowly with time at 1-2 Hz but increasing at 4-10 Hz. This may suggest that the changes in subsurface velocities are depth dependent (i.e., generally increasing at near surface but decreasing at some depth). To further interpret this, we may need to map the frequency-dependent *dt/t* curves to depth-dependent relative velocity changes.

Figure 7b compares the *dt/t* curves measured at a selective of components in the 2-4 Hz band and similar temporal patterns are observed. The consistency between components agrees well with the assumption that the coda waves are dominated by surface (Rayleigh) wave energy. Figure 7c compares the *dt/t* curves measured at station pairs between 2128, 2221, and 5230 in the 2-4 Hz band. While a similar long-term linear trend (velocities slowly decrease with time) for all station pairs, there are some variations in the short-term *dt/t* fluctuations. Furthermore, we also compare the *dt/t* measured using pairs of surface and borehole stations in Figs. 7d-f. While the two *dt/t* curves agree well with each other at 1-2 Hz and 2-4 Hz bands, the results differ significantly at 4-10 Hz band. Since coda waves at 4-10 Hz have much shorter wavelength (likely smaller than the borehole depth), the velocity changes detected by coda waves from borehole stations are associated with structures around the borehole rather than near the surface, which explains the discrepancy observed in Fig. 7f. This is also supported by the observation that *dt/t* at 4-10 Hz band from borehole stations show a long-term linear trend consistent with those at lower frequency bands (Fig. 7d, 1-2 Hz; Fig. 6e, 2-4 Hz).

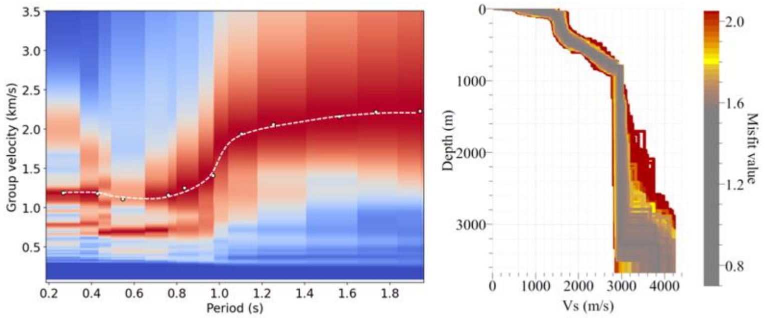

Figure 9: Left: Dispersion diagram of Rayleigh wave group velocity extracted from ANCs computed at Patua. Right: 1-D shear wave velocity inversion using the group velocity dispersion curve (white dashed curve).

The depth sensitivity of surface waves suggests a peak sensitivity at around ⅓ of the wavelength and decay rapidly below one wavelength. Thus, based on the velocity model inverted by fitting the observed surface wave dispersion curve extracted from ANCs at Pauta (Figure 9), *dt/t* measured using coda waves at frequencies above 1 Hz are likely dominated by velocity changes in the top 500 m. Considering the reservoir at Pauta is at the depth of ~1-2 km, despite the poor quality of coda waves at frequencies lower than 1 Hz, we still estimate *dt/t* using the low frequency (0.1-1 Hz) daily ANCs and show the results in Figure 8 to infer velocity changes near the reservoir. In general, uncertainties of *dt/t* measurements are much higher and comparable to fluctuations (~1%) in the *dt/t*. However, we still can see a consistent long-term trend in the *dt/t* suggesting a slowly increasing velocity with time. This linear trend is opposite to those at 1-2 Hz and 2-4 Hz, but similar to (and larger than) that at 4-10 Hz. Assuming all the coda waves are dominated by surface wave energy, the polarity of the linear trend is reversed from 0.2-1 Hz to 1-4 Hz and again from 1-4 Hz to 4-10 Hz, likely suggesting a reversal in long-term changes of velocities at depth. In addition, we also see cycles with shorter intervals (about one month) in *dt/t* at frequencies below 1 Hz, which will be compared to other datasets, such as geodetic and production data, for further interpolation.

5. GPS AND INSAR

In order to understand the stress state and the changes in stress we are monitoring the regional and local deformation and strain around the geothermal field. The primary sources of data are long-term time series from the Global Positioning System (GPS) and shorter-term interferometric synthetic aperture radar (InSAR) measurements from the Sentinel-1 satellite system. The GPS network is regional in scope and the stations are outside of the Patua geothermal field (Figure 10).

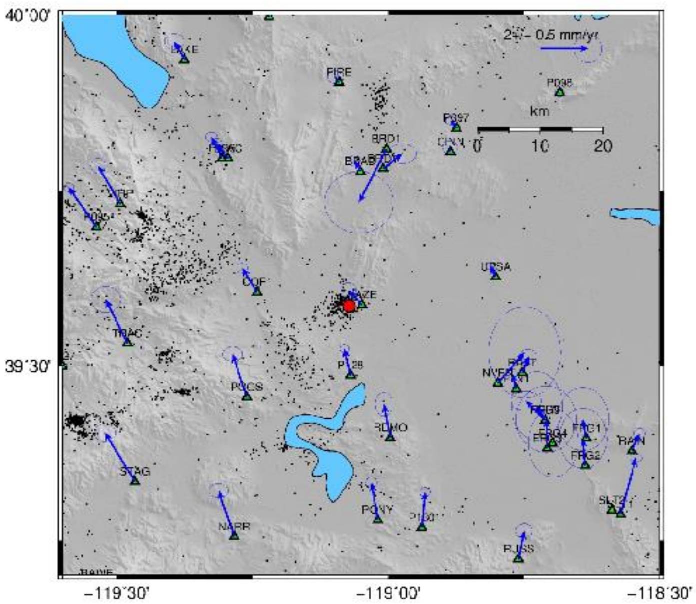

Figure 10: Global Positioning System (GPS) stations in the region surrounding the Patua field (Blewitt et al., 2018). The red dot denotes the location of the field. The blue arrows signify the horizontal displacement.

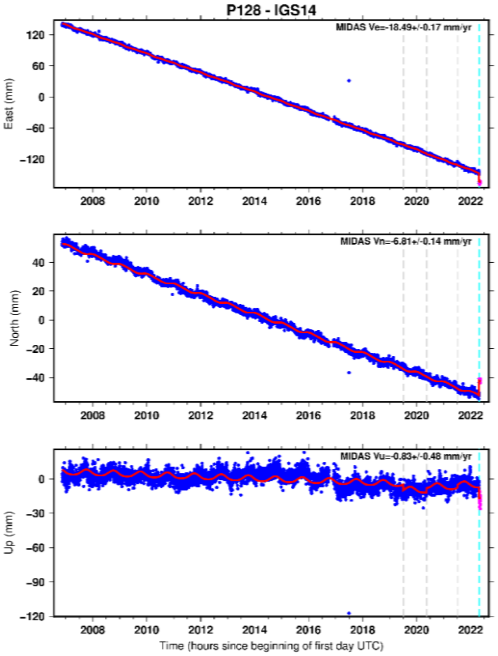

Figure 11: Three components of displacement between 2007 and 2022 for the GPS station P128.

The data have been processed by the Nevada Geodetic Laboratory and the displacements are referenced to a stable North American datum. We have changed the reference point by subtracting the displacement at station P098, which lies in the upper right corner of Figure 10. The long-term deformation is dominated by horizontal tectonic motion as may be seen by considering the three components of displacement at station P128, located about 10 km south of the Patua geothermal field.

The network of GPS stations will be used to determine the regional strain accumulation due to tectonics and will help in determining stress changes due to tectonic loading. We also need to estimate the deformation and stress changes associated with geothermal activities such as injection and production in order to evaluate fracture geometries and permeable pathways in the reservoir, as well as the potential for induced seismicity. Interferometric Synthetic Aperture Radar (InSAR) is a high-resolution technique for estimating surface displacements over time. Satellites make passes over the area of the Patua geothermal field with increasing frequency.

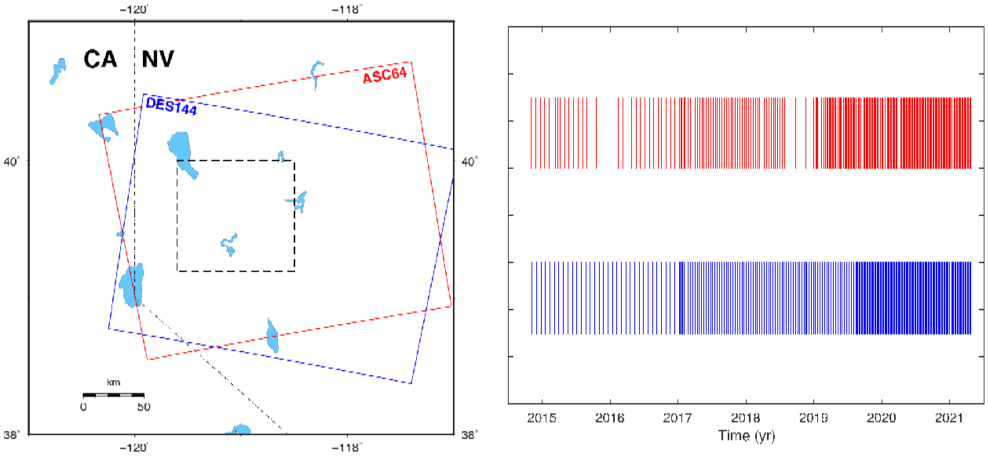

Figure 12: (Left) Ascending track ASC64 and descending track DES144 cover the region encompassing the Patua geothermal field. (Right) The temporal distribution of both tracks as they encounter the area around the geothermal field are denoted by vertical lines. The return time has been reduced to 6 days.

The satellite return time has decreased to 6 days which improves both the temporal resolution of changes and allows for more accurate estimates of displacements over each interval. Using both ascending and descending orbits it is possible to estimate both the vertical and east-west components of surface displacement. For example, in Figure 13 we plot these two components of displacement that occurred between 2018 and 2022.

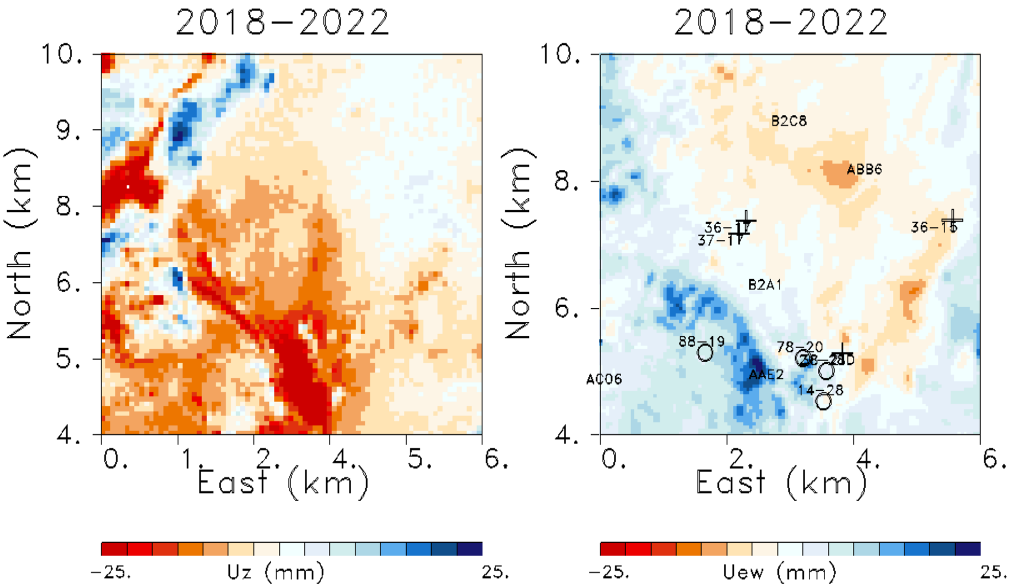

Figure 13: (Left) Vertical displacements between 2018 and 2022. (Right) East-west displacements for the same time interval. Production wells are denoted by open circles and injection wells by crosses.

One difficulty in the Patua area is the significant shallow hydrological signal that dominates the western portion of the area in Figure 13. This is not uncommon in many areas of interest containing either natural or man-made systems such as hot springs or agricultural areas. To get a feel for the magnitude of the problem and a possible solution, consider a transect across the region, as shown in Figure 14. One method that is suggested by the differences in spatial wavelengths of the anomalies in Figure 14 involves wave-number or spatial frequency filtering. That is, deeper sources, such as those in the reservoir some 2 km deep should only have long wave-length surface expressions. As an example, consider the surface deformation associated with the expansion of a single compact grid block at a depth of 2 km, an approximation of an impulse response. The surface deformation and its corresponding wave number spectrum are plotted in Figure 15.

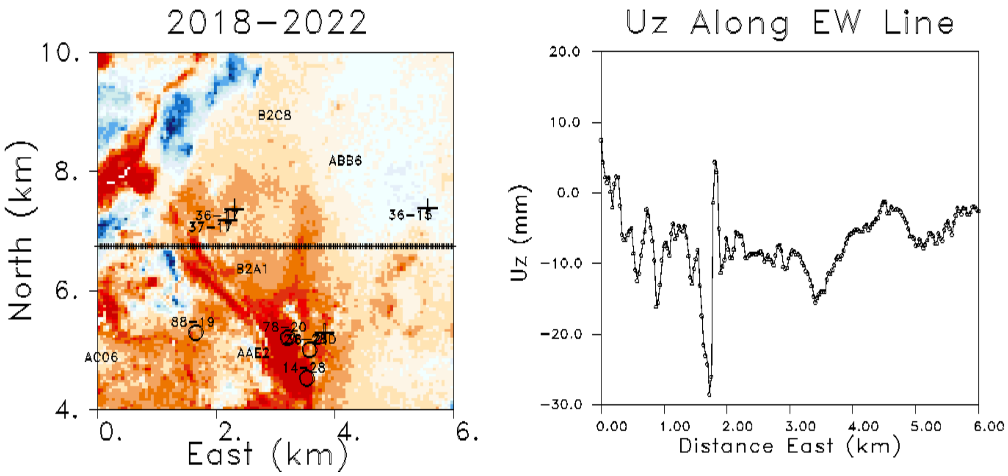

Figure 14: (Left) East-west oriented line over which the vertical displacements are sampled. (Right) Vertical displacement along the line shown in the panel on the left. Note the change in character between changes in the west and in the east.

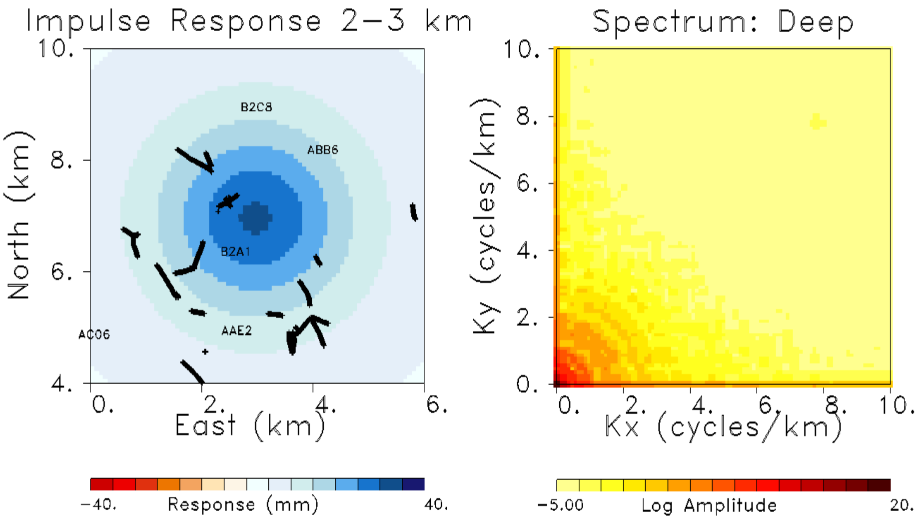

Figure 15: (Left) Surface deformation associated with the volume expansion of a single grid block at a depth of 2.0 km. (Right) Wavenumber spectrum of the anomaly plotted in the left panel.

Such deep sources should have surface wave-lengths of the order of their depth and thus the spatial wave-numbers should be relatively low. The wave number spectrum supports that contention with the largest amplitudes mostly below 2 cycles/km. For comparison we can calculate the spectrum of the vertical deformation shown in Figure 14. In the right panel of Figure 16 we display the wave number spectrum of the vertical displacement field. Note the wider distribution of energy within the spectrum to much large wave numbers.

For a simple comparison we can compare the radial distribution of energy for a shallow source (10-300 m), a deeper source (>2000m), and the observed data (Figure 17). We see that the observed spectrum has higher wave numbers compatible with both deep and shallow sources. Thus, there appears to be a separation in frequency and we can design a filter to remove frequencies that are expected to be small for a source at a depth of around 2 km. We implemented such a filter and applied it to the vertical deformation field shown in Figure 16. The resulting displacement field is plotted in Figure 18 along with the filtered east-west displacement field.

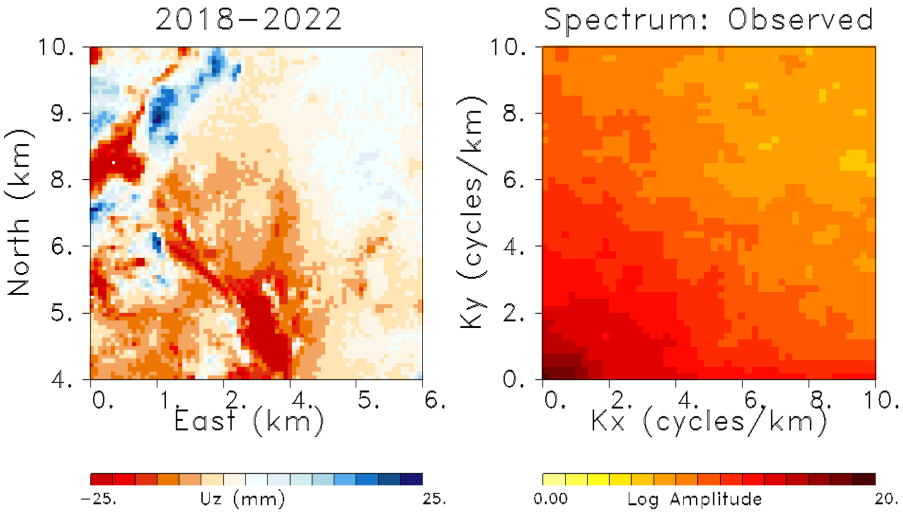

Figure 16: (Left) Observed vertical deformation obtained from the Sentinel-1 InSAR satellite system. (Right) Wave number spectrum of the displacement field.

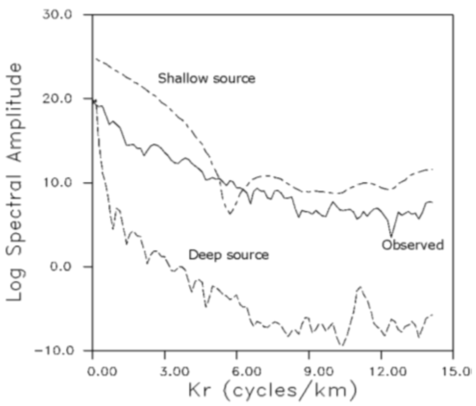

Figure 17: Radial distribution of energy for the wavenumber spectra of displacements due to a deep source, a shallow source, and the actual observations.

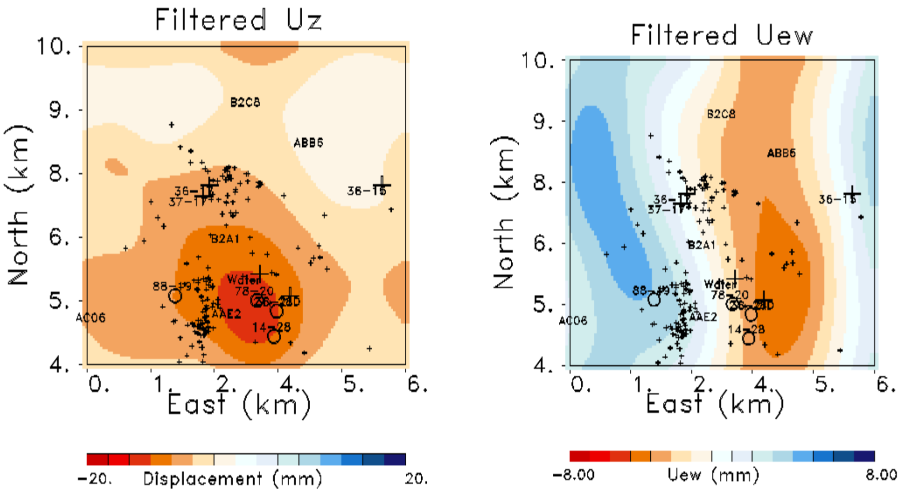

Figure 18: (Left) Vertical displacement field that results from applying a low-pass wave number filter to the observations shown in Figure 13. (Right) Corresponding east-west displacements after filtering the original displacement field.

We can now invert the filtered displacements for volume change at the reservoir depth and try to image the deformation that is induced by injection/production related processes such as poroelastic effects, thermal expansion and contraction, and other effects. We are only estimating the resulting volume change that is produced by these processes, without inferring the exact source of the deformation at this stage. Later we can compare the estimated volume changes with those due to thermal-hydrological-mechanical-chemical modeling, as described below. The inversion method has been described elsewhere (Vasco et al., 2019, Smith and Vasco, 2020) and will not be discussed here. The estimates of volume change for a distribution of grid blocks in a model containing two layers is shown in Figure 19.

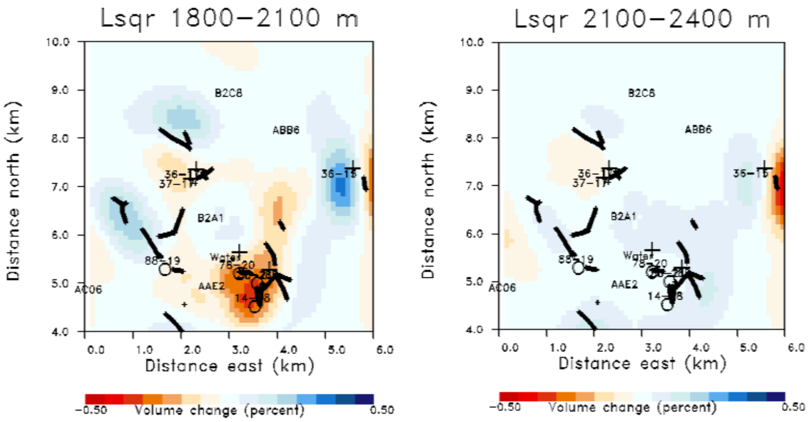

Figure 19: Estimates of volume change distributed in a model of the reservoir. The model is composed of an array of grid blocks distributed in two 300 m thick layers.

As noted above, these estimates of reservoir volume change can be compared with numerical modeling and used to update the reservoir model in an iterative fashion. They can also be used as sources for a geomechanical code to forward model the estimated deformation and stress changes due to reservoir processes. Given the favorable temporal sampling of the Sentinel-1 satellite system we can compute the stress changes for 6-day intervals in many cases. Thus, we can use the estimated stress changes to calculate velocity changes that might be observed by seismic interferometry for the deeper travel paths that are influenced by changes in the reservoir.

6. THMC MODELING

We have re-analyzed fault picks from well logs (Pollack, 2021) combined with drilling lost circulation zone (LCZ) observations (Cladouhos et al., 2017) to find a set of 12 planar segments maximizing a weighting of the number of fault picks and LCZ picks within a 25 m tolerance of the plane segments, fitting 69 of 76 data points. Starting from permeabilities similar to those of Garg et al. (2017) and Murphy et al. (2017) we adjusted them to roughly fit interpolated native state temperature data at two levels; 1005 m below sea level (-1005 m elev., approx. 2250 m depth), and 1107 m elevation (~ 150 m depth over much of the exploited region). A horizontal section of interpreted vertical permeability is shown in Figure 20 (left), and simulated native state temperature at -1005 m elevation is shown in Figure 20 (right).

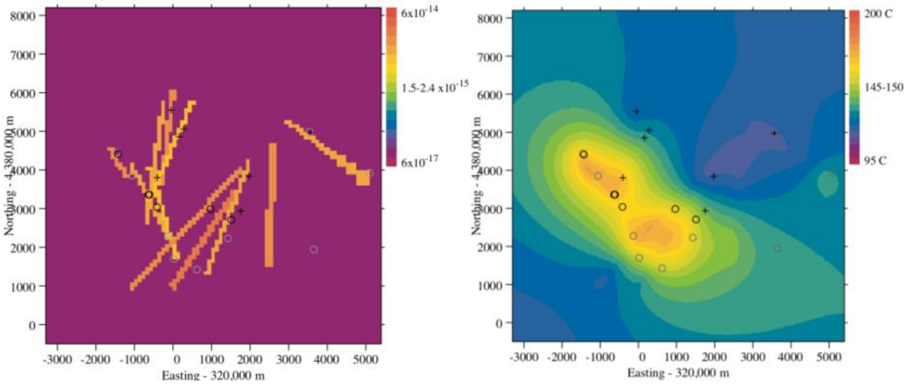

Figure 20: Left: Plan view of vertical permeability at -1005 m elevation. Right: Simulated native state temperatures at -1005 m elevation.

Starting from well logs, we have averaged mechanics parameters such as density bulk and shear modulus, and scaled them to match at the depth of greatest compressional wave velocity, lower frequency measurements on core from Climax stock granodiorite (Stowe, 1969), and subsequently estimated Biot coefficient. Starting from a stress ratio estimate of 0.79: 0.53: 1 from nearby Fallon Air Force Base (Blanksma et al., 2018) we have initialized a stress model, which resolves to a model with higher horizontal stress to vertical stress in declivities, and higher in promontories. Cross sections through Northing 4,383,050 m are shown in Figure 21. Using Mohr-Coulomb fracture criteria the resultant stresses require significant material cohesion to avoid near surface failure. Preliminary efforts at modelling history production at Patua indicates minor creep at depth on existent faults.

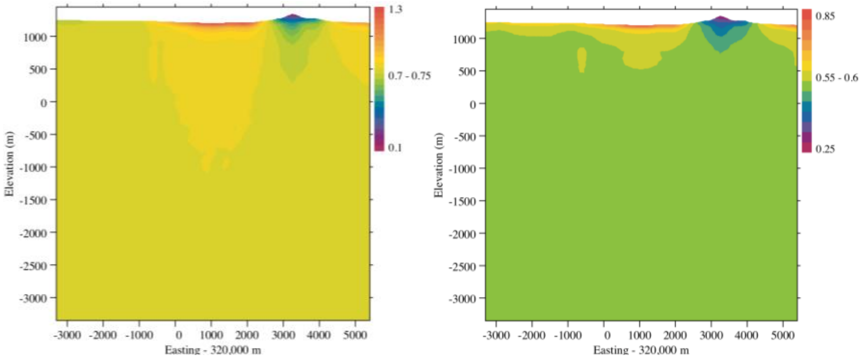

Figure 21: Left: Vertical section of ratio of east-west stress vertical stress at 4,383,050 m Northing. Right: Vertical section of ratio of north-south stress to vertical stress.

7. CONCLUSIONS

We present the current effort of stress characterization at the Patua geothermal field with seismic data acquisition, seismic ambient-noise analysis, InSAR geodesy analysis and volume change inversion, and THMC modeling. The ambient noise shows clear velocity changes in the subsurface, and the low-frequency surface waves contain information at the reservoir depth. The low-wavenumber surface deformation is related to the volume changes in the reservoir, and we apply a wavenumber filter and invert the volume changes. The volume changes are concentrated at the area close to the geothermal plant. This information of subsurface changes can be used to constrain the THMC modeling for more accurate calculation of subsurface stress changes.

8. ACKNOWLEDGEMENTS

We are grateful to Cyrq Energy Inc. for their collaboration to this work. The seismic and well-log data are provided by the DOE Geothermal Technologies Office Wells of Opportunity Amplify project. This work is supported by the U.S. Department of Energy, Office of Energy Efficiency and Renewable Energy (EERE), Geothermal Technologies Office, under Award Number DE-AC02–05CH11231 with Lawrence Berkeley National Laboratory.

REFERENCES

Bensen, G.D., Rizwoller, M.H., Barmin, M.P., Levshin, A.L., Lin, F., Moschetti, M.P., Shapiro N.M., and Yang, Y.: Processing seismic ambient noise data to obtain reliable broad-band surface wave dispersion measurements, Geophys. J. Int., 169, (2007), 1239–1260.

Blanksma, D.J., Blake, K., Pettitt, W., Sabin, A., Varun V., and Damjanac B., 2018. Using Borehole Induced Structure Measurements at Fallon FORGE Combined with Numerical Modeling to Estimate In-Situ Stresses, Proceedings, 43rd Workshop on Geothermal Reservoir Engineering, Stanford, Calif.

Blewitt, G., W.C. Hammond, C. Kreemer: Harnessing the GPS Data Explosion for Interdisciplinary Science, Eos, (2018), 99.

Cladouhos, T.T., Uddenberg, M.W., Swyer, M.W., Nordin, Y., and Garrison, G.H., 2017. Patua geothermal geologic conceptual model, GRC Transactions, Vol. 41.

Combs, J., Peterson, N., Garg, S.K., and Gorenson, C.: Reservoir testing and analysis at the Patua geothermal federal unit, northwestern Nevada, GRC Transactions, 36, (2012), 31–36.

Garg, S.K., Goranson, C., Johnson, S., and Casteel, J.: Reservoir testing and modeling of the Patua geothermal field, Nevada, USA, Proceedings World Geothermal Congress 2015, Melbourne, Australia, (2015).

Lobkis, O.I., and Weaver, R.L.: Coda-wave interferometry in finite solids: recovery of P-to-S conversion rates in an elastodynamic billiard, Phys. Rev. Lett., 90(25 Pt 1), (2003).

Moreau, L., Stehly, L., Boue, P., Lu, Y., Larose, E., and Campillo, M.: Improving ambient noise correlation functions with an SVD-based Wiener filter, Geophys. J. Int., 211, (2017), 418–426.

Murphy, J., Holt, R., and Morrison, M.: A numerical model case study of the Patua geothermal field, GRC Transactions, 41, (2017).

Smith, J.T., and Vasco, D.W.: Adjoint-based inversion of geodetic data for sources of deformation and strain, Journal of Geophysical Research, 126, (2021), 1-12, e2021JB021735.

Pollack, A., Cladouhos, T.T., Swyer, M.W., Siler, D., Mukerji, T., and Horne, R.N.: Stochastic inversion of gravity, magnetic, tracer, lithology, and fault data for geologically realistic structural models: Patua geothermal field case study, Geothermics, 95, (2021), 102129.

Vasco, D.W., Farr, T.G., Jeanne, P., Doughty, C. and Nico, P.: Satellite-based monitoring of groundwater depletion in California's Central Valley, Scientific Reports, 9, (2019), 1–14.